COMMUNICATION

Check for updates

Physiological sensing system integrated with vibration sensor and frequency gel dampers inspired by spider†

Jianren Huang, [iD] [a] Anbang Chen,[a] Jinrong Liao,[b] Songjiu Han,[a] Qirui Wu,[a] Jiayu Zhang,[a] Yujia Chen,[a] Xiandong Lin[b] and Lunhui Guan [iD] *[a]

Recent advances in bioelectronics in mechanical and electrophysiological signal detection are remarkable, but there are still limitations because they are inevitably affected by environmental noise and motion artifacts. Thus, we develop a gel damper-integrated crack sensor inspired by the vibration response of the viscoelastic cuticular pad and slit organs in a spider. Benefitting from the specific crack structure design, the sensor possesses excellent sensing behaviors, including a low detection limit (0.05% strain), ultrafast response ability (3.4 ms) and superior durability (>300 000 cycles). Such typical low-amplitude fast response properties allow the ability to accurately perceive vibration frequency and waveform. In addition, the gel damper exhibits frequency-dependent dynamic mechanical behavior that results in improved stability and reliability of signal acquisition by providing shock resistance and isolating external factors. They effectively attenuate external motion artifacts and low-frequency mechanical noise, resulting in cleaner and more reliable signal acquisition. When the gel damper is combined with the crack-based vibration sensor, the integrated sensor exhibits superior anti-interference capability and frequency selectivity, demonstrating its effectiveness in extracting genuine vocal vibration signals from raw voice recordings. The integration of damping materials with sensors offers an efficient approach to improving signal acquisition and signal quality in various applications.

New concepts

Advanced bioelectronics, particularly wearable devices, have shown great promise in detecting and measuring human physiological signals. Researchers have developed various wearable or implantable flexible vibration sensors based on different sensing mechanisms, allowing for the accurate acquisition of physiological data related to vibration during human–machine interactions. However, these sensors often record signals contaminated by artifacts and noise, necessitating optimized analysis algorithms for noise removal, which can cause partial distortion and delay. Inspired by spider-specialized slit organs and damping structures with cuticle pads, we explored the potential of spider-inspired sensory systems for wide-ranging and heightened vibration detection. By integrating slit-inspired sensors and gel damping mechanisms, a novel strategy was proposed to fabricate a physiological sensing system with a high signal-to-noise ratio. The crack-based sensor exhibits excellent sensitivity and precise perception of vibration frequency and waveform, while the gel damper effectively attenuates external artifacts and noise, ensuring cleaner and more reliable signal acquisition. The integration of damping materials with sensors offers an efficient approach to improving signal quality and anti-interference capability, holding significant potential in various applications, including acoustic analysis and speech research.

1. Introduction

Advanced bioelectronics, particularly wearable and implantable devices, have shown tremendous promise in the field of continuous detection and measurement of human physiological signals.[1,2] To obtain accurate physiological data on frequency, amplitude, and mode related to vibration during human–machine interaction, researchers have developed a series of wearable or implantable flexible vibration sensors based on different sensing mechanisms, such as piezoelectricity,[3] piezoresistance,[4,5] friction electricity,[6–8] capacitance,[9] and photoelectric effect.[10] These sensors have been applied in the fields of human health monitoring of mechanical and electrophysiological signals. However, most reports have focused on the synthesis, design, and preparation of sensitive materials to acquire sensing units with high sensitivity. However, the signals recorded from these sensors often contain artifacts caused by unexpected human activities and environmental noise, such as heart rate signals during walking and respiratory frequency during singing. To selectively remove these extra interferences embedded in dynamic signals, the existing approach relies on utilizing optimized analysis algorithms,

[a] CAS Key Laboratory of Design and Assembly of Functional Nanostructures, Fujian Key Laboratory of Nanomaterials, Fujian Institute of Research on the Structure of Matter, Chinese Academy of Sciences, Fuzhou 350108, China.
E-mail: guanlh@fjirsm.ac.cn

[b] Laboratory of Radiation Oncology and Radiobiology, Fujian Medical University Cancer Hospital, Fujian Cancer Hospital, Fuzhou 350014, China

† Electronic supplementary information (ESI) available. See DOI: https://doi.org/10.1039/d3mh01719b

such as bandpass filtering and high-pass filtering,[11] to deliberately select discrete information and filter out noise signals. However, signal processing by algorithms may cause partial distortion and cannot selectively acquire target frequency bands. Moreover, the corresponding signal delays and lags can occur in additional signal transmission and analysis processes.[12]

Spiders have specialized sensory organs called slit organs on their legs, which are involved in detecting vibrations and air movements.[13] The slit geometry allows sensitive deformation recognition by enabling mechanical compliance, which can detect the small deformation of the slit in response to vibrations in their surroundings.[14] In addition to their sensitive slit organs, spiders have a unique damping system that includes cuticle pads, which play a crucial role in their survival and hunting strategies. The cuticle pad in spider vibration receptors has damping and shock-absorbing properties, allowing spiders to detect small vibration signals caused by prey under windy and rainy conditions.[11] Through the acquisition of high-precision vibration signals by crack-shaped slit organs and selective frequency filtering by the viscoelastic keratin layer, spiders can distinguish and identify target vibration characteristics from intrinsic noise in the environment, achieving a physical filtering effect.

The combination of slit organs and the damping structure with cuticle pads gives spiders a sophisticated and finely tuned sensory system. Numerous researchers have focused on the potential of spider biological sensory systems, which enable wide-ranging and heightened vibration detection.[15–17] Specifically, spider slit-inspired sensors contribute to ultra-sensitivity.[18] Moreover, intrinsically stretchable elastic materials for substrates improve hysteresis, response time, and sensing range.[19] Despite recent progress in ultra-sensitivity spider bionic sensors by introducing slit structure, few studies have focused on improving their damping capabilities to isolate or eradicate the disruptions caused by signals unrelated to the target. Gel damping exhibits viscoelasticity similar to that of the spider's cuticle. Gel damping refers to the utilization of gel materials within sensor systems to mitigate or suppress interference and noise in signals.[20] By leveraging the viscoelastic properties of gels, this approach can effectively attenuate external perturbations and reduce undesired vibrations or oscillations that may otherwise compromise the accuracy and precision of signal measurements.[21] The application of gel damping in biological signal monitoring encompasses diverse domains, and these gel-based damping mechanisms have the potential to minimize motion artifacts, electrical noise, and environmental disturbances, thereby facilitating the acquisition of more robust and artifact-free biological signals.

Above all, the integration of flexible vibration sensors and biomimetic selective dampers enables high-precision signal acquisition and physical filtering, leading to the acquisition of signals with a high signal-to-noise ratio (SNR). Hence, inspired by the spider's organ, we proposed a novel strategy involving the utilization of nanomaterial-loaded crack-based sensors to fabricate a physiological sensing system integrated with frequency gel dampers. The presented crack sensor exhibits high sensitivity with an excellent gauge factor of 28 510, and the sensor effectively detects and measures small to large changes in strain in a wide sensing range of 0–800%. Its remarkable ability to accurately perceive the vibration frequency and waveform makes it a promising sensory device for detecting bioelectronic signals. Pad-inspired gel-damping materials have been demonstrated to enhance the stability and reliability of sensors by providing shock resistance and isolating external factors. Gel damping effectively attenuates external motion artifacts and low-frequency mechanical noise, resulting in cleaner and more reliable signal acquisition. By integrating the gel damper with a crack-based vibration sensor, the combined sensor exhibits superior anti-interference capability and frequency selectivity. The gel-damped integrated sensor proves effective in extracting genuine vocal vibration signals from raw voice recordings, demonstrating its potential to enhance acoustic analysis and speech research. The integration of damping materials with sensors offers an efficient approach to improve signal acquisition and signal quality in various applications.

2. Results and discussion

2.1 Structural design and working mechanism of the spider-inspired sensing system

Spiders are fascinating creatures, and their ability to sense and interpret vibrations is a crucial part of their survival and reproductive strategies.[13] They have evolved specialized vibration detectors that allow them to perceive and respond to various environmental cues, particularly those related to their prey, potential threats, and mating opportunities (Fig. 1a).[22] As shown in Fig. 1b, when an external force, such as vibration, is applied to the leg, it causes the slits to close through compression. By emulating the structure and adjusting the mechanism of the slit organ, we created a sensor that exhibits non-linear changes in electrical resistance when subjected to deformation. This effect is achieved by introducing micro cracks onto a flexible conductive film (Fig. 1c). The exceptional sensitivity of the sensor enables an adjustable and dynamic sensing range, allowing it to monitor frequencies and amplitudes across various scales with remarkable precision. In addition, the vibration sensors are composed of a cuticular pad with specific properties. The pad contains parallel slits that are embedded in the spider's cuticle and are covered by an outer membrane (Fig. 1d). The cuticular pad exhibits viscoelastic damping behavior owing to the presence of viscous hydrogen bonds between the chitin (a component of the spider's exoskeleton) and protein chains within the pad.[23] In the context of viscoelasticity in Fig. 1e, the material exhibits both viscous (fluid-like) and elastic (solid-like) characteristics. This means that the cuticular pad responds to vibrations by deforming slightly and then returning to its original shape. As illustrated in Fig. 1f, this viscoelasticity allows the pad to respond differently to vibrations of varying frequencies. When the applied vibration frequency is above a certain threshold (low frequency), the pad changes from a rubbery state to a glassy state. The phase
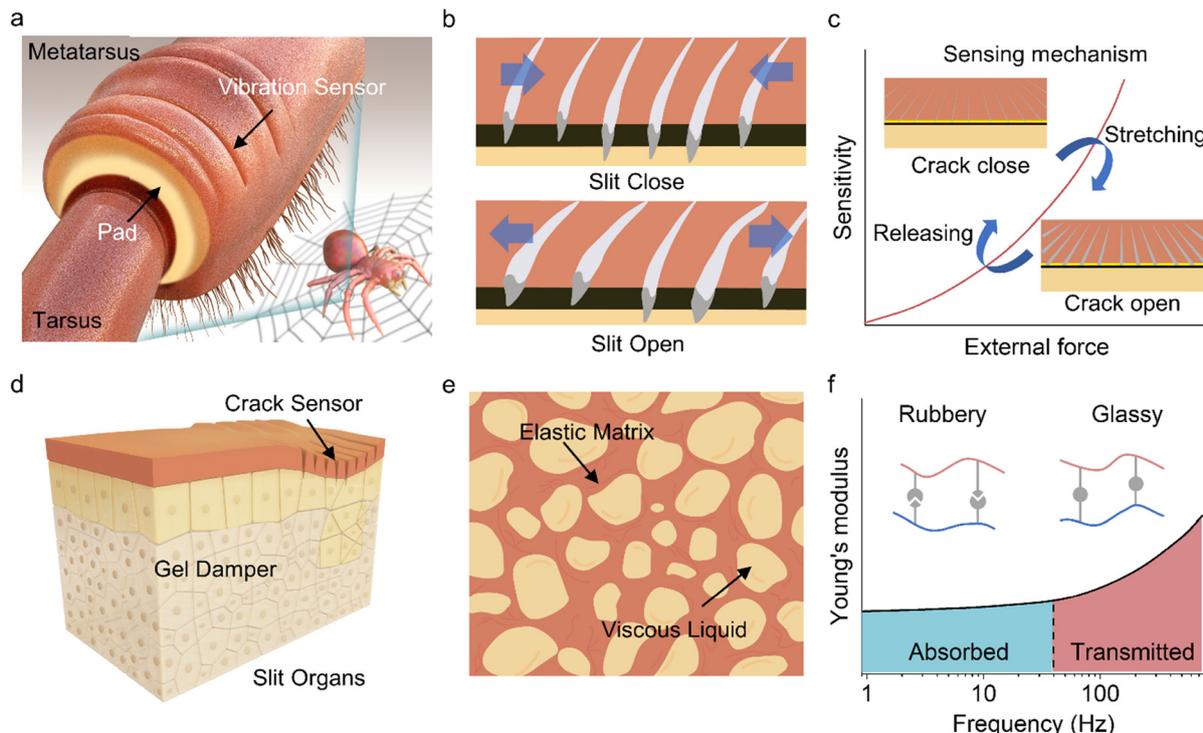
Fig. 1 Structural design and working mechanism of the spider–inspired sensing system. (a) Amping in a spider's cuticular pad between and vibration sensor in lyriform slit organs. (b) Schematic illustration of the morphological features of the slit organ. (c) Morphological feature–inspired sensing mechanism of the crack sensor along the opening and closing of the crack. (d) The slits are in a highly stiff exoskeleton (surface) and a viscoelastic pad (below the exoskeleton). The slits (crack sensors) are connected to the pad (gel damper) to monitor vibrations. (e) Schematic illustration of the structural features of the cuticular pad. (f) Viscoelastic properties of the spider's pad, which depend on the applied frequency of vibration.

transition facilitates the pad in selectively transmitting target vibration signals while effectively filtering out low-frequency noise. By combining the damping properties of the cuticular pad and the structure of the selective vibration detectors, spiders can effectively separate important vibration signals from the background noise. This enables them to focus on crucial cues related to their prey, predators, and potential mates, even under adverse conditions, such as windy or rainy environments.

By investigating the structure and mechanisms of the selective vibration detectors of spiders in detail, a spider-slit-organ inspire sensor system is designed.[24] The fabrication process of the bioinspired vibration sensors based on the micro crack structure is described in detail in the experimental section and ESI.† Thermoplastic polyurethanes (TPUs) with flexibility, durability, and biocompatibility were selected as materials to prepare the foundation of the sensors. The TPU substrate was freshly produced by electrospinning, leading to the formation of a structurally deformable elastic fiber web (Fig. S1 and S2, ESI†). To endow the electrical response properties, stable MXene ink was prepared to be assembled (detail in the ESI† of Fig. S3–S5). Plasma treatment was applied to improve the hydrophilicity of the TPU substrate surface (Fig. S6, ESI†), thereby enhancing adhesion and avoiding delamination of the conductive layer on the substrate.[25] After vacuum filtration deposition, MXene was coated on the surface of the electrospun

TPU fibrous membrane, forming an electrically conductive layer on the surface, and the microcracks structure was then constructed by pre-bending (Fig. S7, ESI†).

The MXene-loaded content in the samples was calculated by performing TGA analysis, demonstrating that approximately 30% of the composite structure was composed of filtered MXene (Fig. S8, ESI†).

The typical (002) peak of the MXene nanosheet was observed in the X-ray diffraction analysis (XRD) plots of MXene@TPU, demonstrating that MXene was successfully loaded in the TPU fiber network (Fig. S9, ESI†). As further shown in Fig. S10 (ESI†), the cross-sectional scanning electron microscope (SEM) image and the energy dispersive spectroscopy mapping of the MXene@TPU film exhibited a stable network structure by tightly wrapping the MXene nanosheets with TPU fiber. The fiber network coated in the conductive layer can conduct electricity in the deformed state (Fig. 2ai and Fig. S11, ESI†). Then, excess MXene flakes continuously accumulated on the fiber network surface and formed thin films through self-assembly (Fig. S12, ESI†). This MXene layer on the TPU was mechanically bent with a curvature rod, which provides a consistent curvature to ensure uniform crack formation (Fig. S13, ESI†). Cracks generated by bending stress exhibited straight and perpendicular alignment with the direction of stress. After pre-treatment, the material displayed a multiscale pattern of jagged microcracks that resembles the structure of a slit organ (Fig. 2aii).[17] A highly
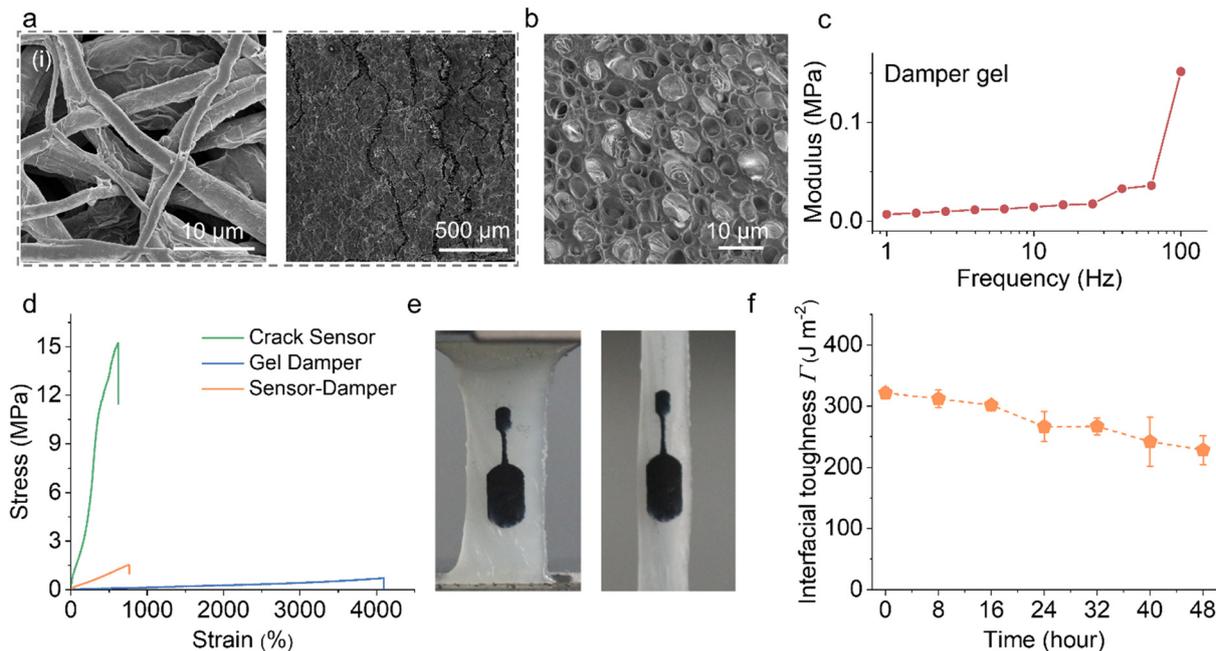
Fig. 2 (a) Structure characterizations of a prepared crack sensor, (a(i)) SEM image in cross-sectional. (a(ii)) SEM in surface view. (b) SEM image of the gel damper. (c) Dynamic mechanical test of the gel damper. (d) Typical tensile strain–stress curve of gel damper, crack sensor, and integrated device. (e) Photographs show superior adhesion between the sensor and damper layers. (f) Interfacial toughness between the gel damper and the crack sensor measured 48 hours after adhesion formation.

controllable method in terms of crack density and direction yields reproducible electrical signals. Detecting changes in electrical conductivity when cracks are open or closed allows them to be employed in vibration-sensing applications.

To design and integrate a damping system into the fabricated bionic crack sensor, specifically targeting the absorption of low-frequency noise vibrations while preserving the target signal, we fabricated a polyacrylamide acrylic (PAMAA) and gelatin interpenetrating gel damper.[26,27] It was observed that the gel damper exhibited a specific cuticular pad structure in the SEM image of Fig. 2b and the optical image of Fig. S14 (ESI†). The closely connected cell shapes a polymer chain from the elastic tissue (high Young's modulus) that experiences external force deformation while being filled with a viscous binary solvent as dissipating elements, together contributing to damping capacity. As low-frequency vibrations passed through the damper, the viscous (liquid-like) characteristics acted as a damping mechanism, converting mechanical energy into heat, which reduced the amplitude and intensity of the vibrations.[28] The elastic (solid-like) characteristics of the viscoelastic gel damper material ensured that the gel damper could deform slightly in response to vibrations and then recover to its original shape once the external force was removed. This resilience allows the sensor to quickly reset itself after exposure to vibrations, ensuring that it remains sensitive to subsequent signals.

The elevated modulus achieved a transition from viscosity to elasticity of the gel damper, allowing for the elastic transmission of vibrational signals. To comprehensively investigate the vibration-dependent dynamic behavior of the gel damper, we plotted the frequency-module curves at a reference temperature of 25 °C (Fig. 2c). Similar to the cuticular pad of a spider, the curves can be classified into two regimes with increasing frequency: rubbery and glassy. When the frequency gradually increased, the modulus of damping started to rapidly increase at approximately 20 Hz. The damping transformed from a rubbery state to a glassy state.

The gel damper integrated crack vibration sensor required stable mechanical performance and a firm interface bond. Fig. 2d demonstrates that the gel damper exhibits high stretchability, with maximum elongations reaching approximately 4000% without reaching the breaking point. Furthermore, at higher strains, no strain softening or stress declination occurred. The nanoscale layered structure of montmorillonite formed colloidal particles in the gel, creating an interlocking structure through interactions with water molecules. This helped alter the gel's rheological properties and mechanical performance, making it more stable. In addition, by coating the MXene flakes, the TPU fiber substrate exhibited enhanced mechanical properties (Fig. S15, ESI†). Consequently, the high-toughness crack sensor can effectively match the mechanical performance of the damping material and maintain its structural stability during deformation. Consequently, synergistic interfacial bonding can endure significant deformation of up to 300% stretch without experiencing any debonding, as illustrated in Fig. 2e. As shown in Fig. S16 (ESI†), during 100 cycles of stretching and releasing, the integrated sensors demonstrated stable mechanical behavior. The mechanical curve did not observe fluctuations caused by material interface damage and modulus mismatch. The deformed stability of the device was further investigated by
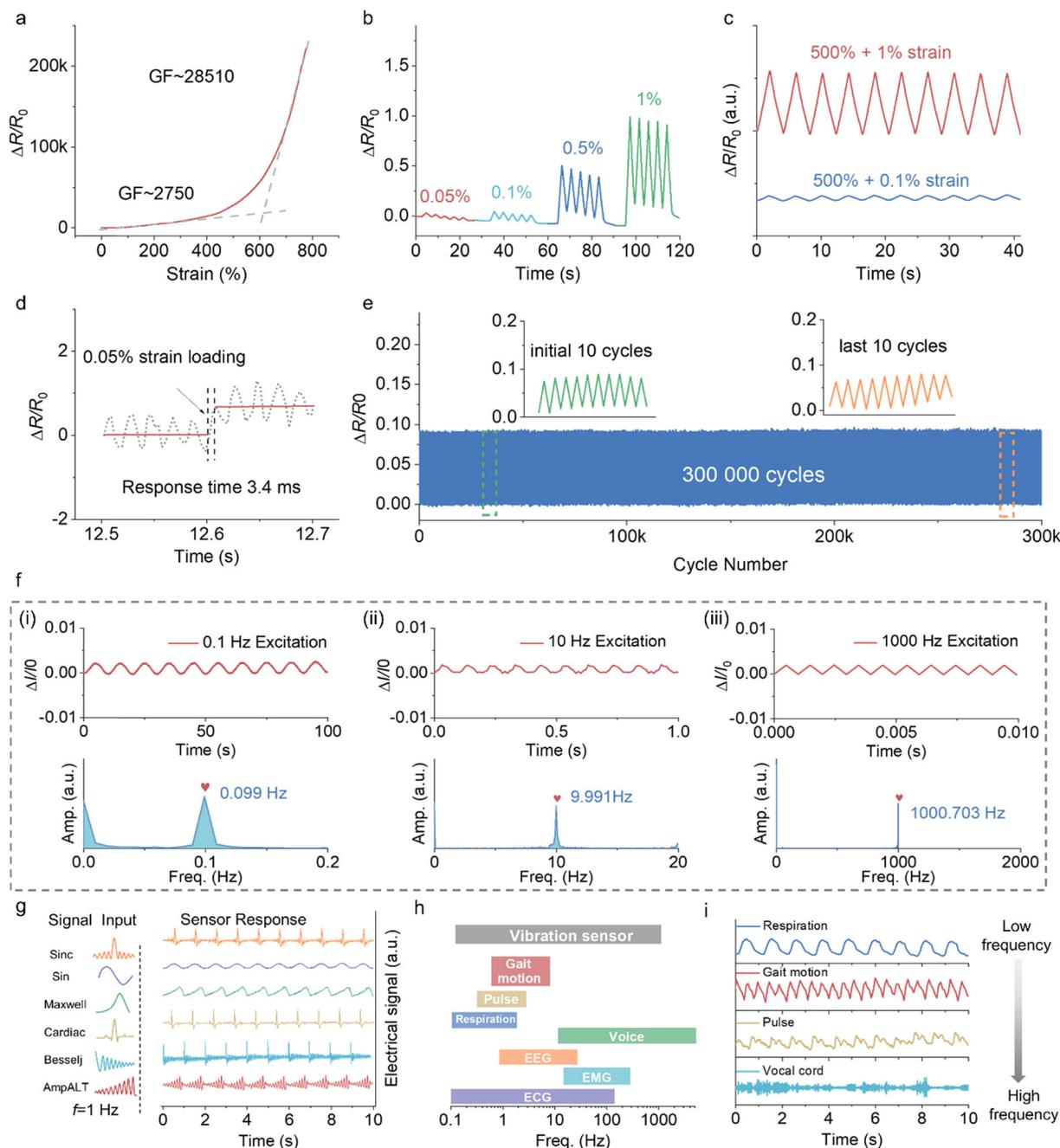
Fig. 3 Static and dynamic electromechanical response performance of the MXene@TPU crack sensor. (a) Relative electrical resistance-strain response signal of the crack sensor. (b) Resistance variation of sensor applied ultra-low tensile strain. (c) Resistance variation of a sensor applied to superimpose 1% and 5% strains on fixed 500% strain. (d) Response time of the sensor with applied 0.05% strain. (The raw signal was notch filtered at 50 Hz). (e) Durability test of the sensor through 300 000 loading and unloading cycles at 100 Hz mechanical vibration. (f) Electrical signal variation of the crack with different vibration frequencies (0.1 Hz, 10 Hz and 1000 Hz) and the corresponding FFT-processed frequency spectrum. (g) Recognition of the sensor to different input mechanical vibration waveforms. (h) Representative frequency ranges of human mechanical, electrophysiological biosignals and vibration sensing ranges. (i) Recognition of the sensor to different input biosignal frequencies.

performing a peeling experiment to test the interfacial toughness of the crack sensor bond to the damper layer *via* adhesive properties.[29] Fig. 2f illustrates that the sensor layer can establish robust adhesion to the damper upon contact, resulting in an interfacial toughness of 321 J m^{-2}. However, when the adhered sample was exposed to an open-air atmosphere, the interfacial toughness decreased to 228 J m^{-2} over a period of 48 hours. The increase in interfacial toughness can be attributed to the high viscosity of glycerin, promoting stronger interfacial interactions.[30] Despite the existence of a modulus mismatch, the sensing system maintained a stable and durable interface. Through the rational structural design of the crack sensor

and gel damping, we obtained an integrated vibration sensing system.

2.2 Static and dynamic electromechanical response performance of the crack sensor

Spider's slits are highly sensitive and can capture faint vibration signals from a distance. Inspired crack sensors require high sensitivity to perceive subtle vibrations in complex environments. Therefore, the response capability of the crack sensor to vibration was systematically studied under controlled conditions, subjecting it to various types of mechanical stimuli that mimic real-world scenarios. Fig. 3a demonstrates that the crack sensor exhibited a significant increase in resistance change in response to applied loading, which is typical behavior for a force/strain sensor. The relationship between the applied force and the resulting resistance change was used to determine the sensitivity of the sensor. The sensitivity (quantified by GF) of the sensor was calculated as 28510 in a sensing range of 0–800%.

This means that even with a wide sensing range of 0–800%, the sensor can effectively detect and measure small or large changes in strain. This level of sensitivity makes the crack sensor suitable for a broad range of sensing applications.

We investigated the crack structural evolution of a sensor under various strains by conducting an *in situ* stretching test to understand the sensing mechanism. Changes in the conductive network were primarily attributed to the development of cracks during deformation. Specifically, at a small tensile strain, the 2D MXene flakes played a crucial role.

As illustrated in the *in situ* SEM image of Fig. S17 (ESI†), the presence of cracks resulted in a decrease in the number of contact joints between neighboring 2D MXene flakes, consequently hindering electron transfer and resulting in a sensitive response. As the strain increased, a greater number of cracks were generated, causing continuous damage to the conductive channel, which results in a gradual increase in resistance. Fig. S18 (ESI†) illustrates that when the deformation was consistently applied, the MXene-coated TPU fiber acted as a bridge connecting the divided MXene flakes and facilitating electron transport. This configuration contributed to an ultrahigh GF and an enlarged sensing range for the sensor. The use of conductive fiber allowed the sensor to tolerate large deformations while maintaining structural stability. The cracked sensor exhibited an obvious increase in resistance with high repeatability when subjected to loading, producing up to 200% strain, and subsequently returned to its initial state (Fig. S19, ESI†). The corresponding cycle of resistance change demonstrated that the loading/unloading was nearly reversible with ultralow hysteresis within a border working range, which was a desirable characteristic of functional sensors.

Afterward, the sensor's response to electrical signals was assessed under ultralow strain conditions to investigate its ability to function as a vibration sensor with the capacity to sense low amplitudes. As depicted in Fig. 3b, a series of cyclic sensing experiments were carried out at ultralow stretch strains. The results showed that the sensor exhibited remarkable sensitivity, and even at an extremely low strain of 0.05%, it generated stable electrical signals that could be accurately recorded. The incorporation of 2D MXene confers an ultralow detection limit to the sensor, which is primarily attributed to the sensitive contact between the nanosheets within the crack structure.

Traditional rigid sensors face a significant challenge in simultaneously detecting both large and subtle strains. To demonstrate the remarkable response behavior of our sensor, we conducted reversible stretching experiments on the sensor from 100 to 500% strain (Fig. S19 and S21, ESI†), along with an additional slight amplitude. Surprisingly, even when subjected to a tensile strain of 500%, the sensor can still capture and distinguish slight strains of 1% and 5%, demonstrating its ultrahigh operating sensory resolution (Fig. 3c). The Mxene-coated TPU fiber network, which serves as the skeleton, is advantageous because of its wide strain range and excellent sensing stability. This impressive ability to detect and differentiate various strain levels has opened new possibilities for applications in highly sensitive and precise sensing scenarios.

Additionally, the sensor's remarkable sensing ability to even subtle changes in strain and its rapid response contribute to achieving a high-frequency sensing resolution. To determine the response time, the sensor's resistance was measured after applying a sudden strain of 0.05%. As depicted in Fig. 3d, the sensor exhibited an ultrafast response time of approximately 3.4 ms during tiny dynamic loading. It is noteworthy that real response times could be even faster than the recorded value, considering the contact duration between dynamic loading and electronics during the experiments (Fig. S22, ESI†). Fig. S23 and Table S1 (ESI†) provide a comparison between the crack sensor and other recent reports, demonstrating that the sensor has one of the lowest detection limits and the fastest response ability among the available options. Moreover, the durability of the sensor was thoroughly tested by subjecting it to 300 000 cyclic strain tests (Fig. 3e). The cyclic test results confirmed the stability of the crack sensor, as it consistently demonstrated a rapid and reliable signal to the applied deformation and returned to its original state after release. The 300 000-cycle durability test was one of the highest values mentioned in the existing literature (Fig. S24, ESI†). Moreover, the repeatability and cyclicity of the sensor under large deformation loads were significant properties for practical applications. The crack sensor underwent a series of cyclic tests involving more than 100 loading and unloading cycles, each subject to a 100% tensile strain, as illustrated in Fig. S25 (ESI†). It consistently demonstrated a rapid and dependable response to applied loads and consistently reverted to its initial state after each stretching and releasing cycle. This remarkable durability ensured its suitability for prolonged and demanding usage scenarios, further reinforcing its potential as an exceptional sensing solution.

The detailed perception process of the spider to surrounding vibrational objects could be divided into sensing the frequency and waveforms of the vibration. Specifically, advanced sensing with ultra-sensitive and full sensing range features was the

prerequisite for vibration recognition. Existing nature-inspired flexible sensors were generally good at detecting slow changes or quasi-static responses in target objects. However, these sensors struggle to detect minute high-frequency oscillations caused by dynamic loading, such as vibrations or rapid changes in stress. By subjecting the crack sensor to controlled dynamic stimulation, its ability to detect and respond to sensing the vibrations can be analyzed. To evaluate the effectiveness of the crack sensor in detecting vibration frequency and waveforms, a dedicated measurement and control system was established. (See details in the experiment section and Fig. S26, ESI†).

We initially investigated the crack sensor's capability to detect the inherent frequency of a cantilever beam. As illustrated in Fig. S27 (ESI†), an impulsive load was applied to the free end of the beam, causing bending stresses at the fixed end, resulting in variations in the electrical signal generated by the sensor. The experimental results in Fig. S28 (ESI†) demonstrated that regardless of changes in the impact location or the magnitude of the applied force, the inherent frequency of the beam could be accurately obtained (error < 2%, accelerometer). The sensor was applied to fixed frequency excitation at frequencies operating in the range of 0.1–1000 Hz to present its capacity to precisely detect dynamic loading variations. As shown in Fig. 3f, the sensor possesses outstanding response ability with distinctly and repeatably waveforms in detecting mechanical vibrations within a broad frequency sensing range. Moreover, the exceptional sensitivity of the sensor endowed it with a higher SRN, allowing it to detect low-frequency (0.5 Hz and 1 Hz) signals beyond the range of a typical accelerometer (Fig. S29, ESI†). Additionally, the sensor exhibited more stable sensing behavior even under high-frequency excitations from 100 to 1000 Hz (Fig. S30, ESI†). As illustrated in the frequency spectrum through the Fast Fourier Transform (FFT) in Fig. 3f, the frequencies extracted for the fixed excitation frequencies of 0.1, 10 and 1000 Hz were 0.099, 9.991 and 1000.703 Hz, respectively, which exactly agreed with the input constant excitation frequencies (with an error of only 0.1%).

To validate the waveform response capacity of the vibration sensor, various types of input vibration waveforms were obtained, such as Sin, Maxwell, Besselj, and Cardiac waves, with a constraint amplitude and a frequency of 1 Hz (Fig. 3g and Fig. S31, ESI†). The output waveforms of the electrical signal changes were similar to those of the input of the signal generator. These vibration sensing properties can be used in bioelectronics. As illustrated in Fig. 3h, the developed vibration sensor demonstrated the ability to detect the vibration frequency within the range of 0.1–1000 Hz, encompassing a wide spectrum that includes most bioelectronic frequencies. In addition to frequency information, the vibration signals also included an important aspect of the waveform. As illustrated in Fig. 3i, the dynamic signal from human motion was detected, from 0.01 to nearly 15 Hz, such as respiration (0.1 to 2 Hz), gait motion (1 to 15 Hz), pulse (0.3 to 4 Hz) signals, and vocal cord vibration (80 to 200 Hz).

2.3 Damping properties and related application in bioelectronics

The shock-resistant performance and damping behaviour of spider-inspired gel damper were characterized and demonstrated and compared the performance with commercially available polymeric dampers for shock absorption (D3O and PDMS). Drop-ball experiments with a steel ball on different damping materials were conducted to assess the elastic transmission and reflection of mechanical energies, representing the shock wave attenuation capabilities (Fig. 4a). The shock progress was monitored by the corresponding change in the accelerometer signal. As illustrated in Fig. 4b and c, the gel damper exhibited superior damping performance and effectively attenuated the propagation and amplitude of shock acceleration peaks associated with the generated shock waves, facilitating rapid deceleration of the steel ball. They can absorb and disperse the energy of mechanical vibrations, decreasing vibration transmission and resonance response, thereby enhancing the stability and precision of the acquisition system. In contrast, PDMS and D3O demonstrated comparatively inferior damping performance.

Besides, gel damping presented certain filtering capabilities, allowing for the absorption of low-frequency noise signals. Its polymeric structure and crosslinked network can attenuate frequency vibrations, enabling the signal acquisition system to perform well in the frequency domain. As illustrated in Fig. 4d, the vibration signal begins to transmit through the gel surface when the frequency increases, with the waveform of vibration recorded in the acquisition devices. Therefore, gel damping can enhance the SNR by absorbing low-frequency environmental noise during the testing process of wearable devices while avoiding the interference of motion artifacts. Gel damping exhibits promising potential for application in the monitoring of biological signals.

To enable the application of gel damper in bioelectronics and continuous biosignal signal monitoring, we conducted relevant tests on their environmental stability, biocompatibility, and skin adhesion. Initially, owing to the incorporation of binary solvents, damping materials exhibited excellent environmental stability, allowing them to operate on the surface of the skin for an extended period without experiencing dehydration. Then, when the gel damper is applied to the skin, biocompatibility is essential to prevent itching and redness of the skin. Human umbilical vein endothelial cells (HUVECs) and BEGM Bronchial Epithelial Cells were used to evaluate the biocompatibility of the samples (see details in ESI†). The cells (HUVECs) were cultured *in vitro* for 1 day, 3 days, and 7 days. After incubation for 7 days, HUVEC proliferated rapidly and indicated similar high cell viability as those in the control group (Fig. 4e). No statistically considerable differences in the OD values for the two cases were recorded (Fig. 4f), suggesting the low cytotoxicity and outstanding biocompatibility of the gel damper. Besides, the prepared gel damper required seamless contact and outstanding adhesion to the skin surface. As introduced in Fig. S32 (ESI†), the adhesive strength of the gel damper when attached to different substrates is compared.
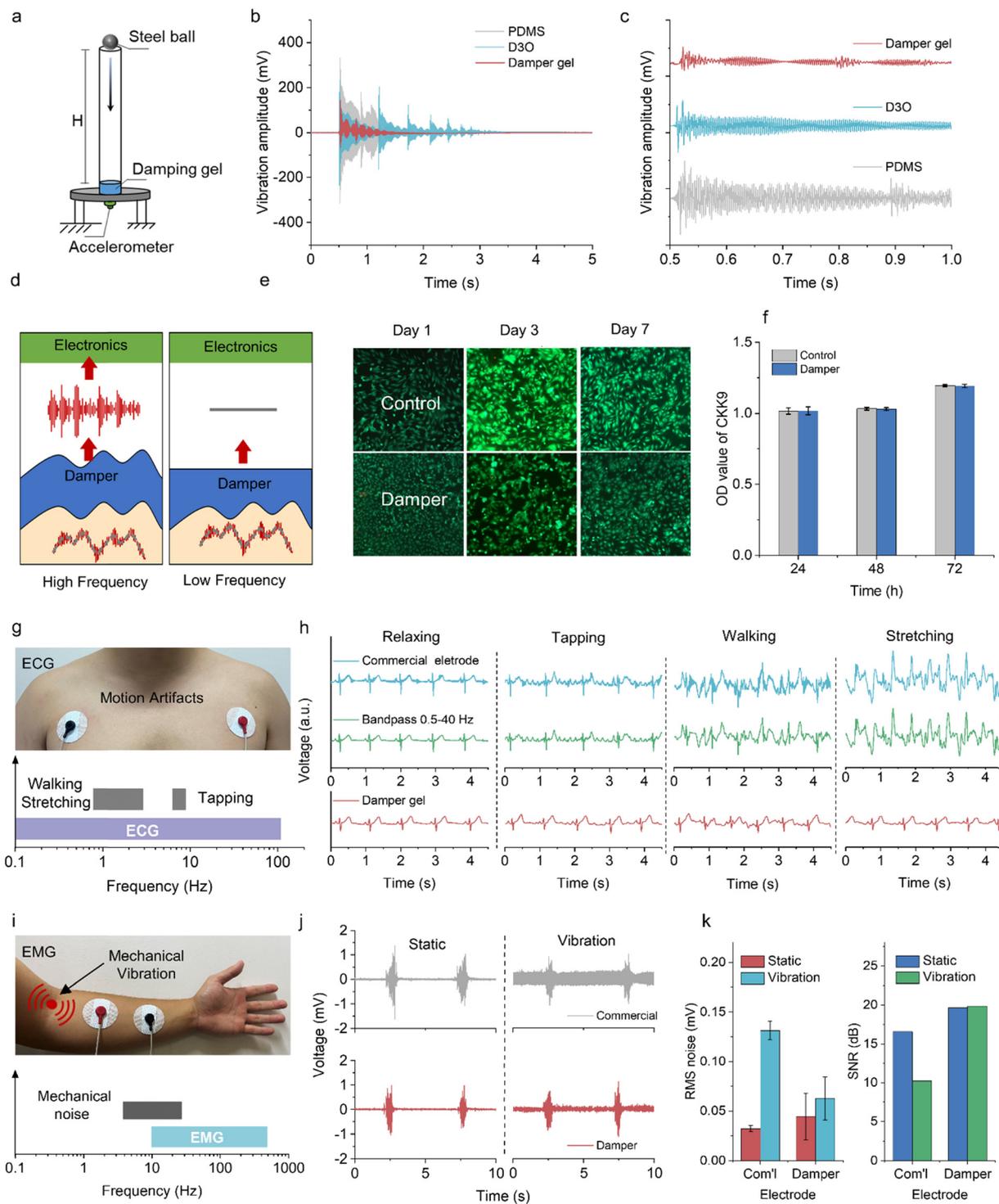
Fig. 4 Damping properties and related applications in bioelectronics. (a) Experimental configuration diagram for evaluating gel damper performance in shock control test. (b) and (c) Time-dependent vibration waves observed with the D3O, PDMS, and gel damper when a steel ball was dropped freely from heights of 1 m. (d) Schematic illustration of biophysiological signal detection through the hydrogel damper from the skin and surroundings. (e) Fluorescent image of HUVECS cultured in samples. (f) CKK9 assay was performed to determine the proliferation of HUVECS inoculated on the samples. (g) Demonstration of ECG recording based on a gel damper electrode (commercial 3 m electrode as a reference). (h) ECG signals recorded by a commercial electrode, after bandpass filtering (from 0.5 to 40 Hz) and using the gel damper electrode in various motion states. (i) Demonstration of EMG recording based on a gel damper electrode (commercial 3 m electrode as a reference). (j) EMG signal recorded by damper gel and commercial electrodes in normal and vibration states. (k) The corresponding baseline noise and the signal-noise ratio of the EMG signal.

The characteristic lap–shear curve showed that the adhesive strength ranges from 19.2 kPa for PTFE to a maximum of 121.6 kPa for wood. Moreover, as depicted in Fig. S33 (ESI†), the gel damper formed a tight bond with the human skin, enabling the skin to deform freely and reversibly in various deformations without any detachment of the gel damper. Importantly, there were no signs of redness or residue when the sample was removed from the skin. The strong adhesion and ultra-low elastic modulus of the damper facilitated the formation of conformal skin-electrode interfaces, which helped in maintaining contact impedance. (Fig. S34, ESI†)

Gel damping exhibited outstanding comprehensive performance. Hence, the incorporation of gel-damping techniques in the field of biological signal monitoring has considerable potential for enhancing signal quality and reliability. Integration with a gel damper material on commercial Ag/AgCl electrodes can be used to acquire electrophysiological signals. By leveraging the viscoelastic properties of gels, this approach can effectively attenuate external perturbations and reduce undesired motion artifacts or mechanical vibration oscillations that may otherwise compromise the accuracy and precision of signal measurements.

The motion artifact is one of the significant challenges for flexible sensors in acquiring target signals. The robustness of the damper against motion artifacts is assessed and explored to obtain high-quality electrophysiological signals of ECG. Two electrodes, namely a commercial 3 M and a gel damper electrode, were used for the investigation and attached to the chest of the volunteer as working electrodes to detect ECG signals (from 0.1 to 150 Hz) (Fig. 4g). ECG signal monitoring was performed in a state of relaxation and movement. The motion included tapping, walking, and stretching in chest expansion, implying that the exercise frequency ranged from 1 to 10 Hz. When the representative signals after motion artifact application were evaluated, interference noise obscured the ECG signal waveforms, whereas the ECG waveforms were recorded in the gel damper electrode regardless of motion movement (Fig. 4h). The commercial gel electrode failed during intense exercises, such as chest expansion. Bandpass filtering ranging from 0.5 to 40 Hz proved ineffective in all cases owing to the frequency of motion noise that overlapped with the frequency ranges of the target signals. In contrast, the gel damper results displayed steady and distinctly representative signals unaffected by external noise. These findings suggest that the gel damper electrode outperforms the 3 M gel electrode in mitigating motion artifacts.

The low-frequency mechanical vibration noise of the surrounding environment significantly influenced the external factors of the signal acquisition, thereby reducing the purity and reliability of the acquired signals. To assess the properties of the gel damper in environmental isolation, a low-frequency mechanical vibration noise was applied to induce forearm movement EMG signal (10–500 Hz), near the working electrodes. As depicted in Fig. 4i, the gel damper electrode patch was attached to the forearm of a volunteer to acquire EMG signals. Vibration was implemented by applying a vibrator (5–20 Hz),

and commercial 3 M hydrogel electrodes acted as a reference. EMG signals measured by gel damper electrodes and commercial samples were recorded under both static and dynamic conditions, as depicted in Fig. 4j. When the fist was clenched in a static state without mechanical noise, high-quality EMG signals were recorded by employing both the gel damper and commercial 3 M electrodes. As calculated in Fig. 4k, the SNR of the signals recorded by the gel damper (26.88 dB) was similar to that of commercial electrodes (25.95 dB). To assess mechanical noise, the root-mean-squared (RMS) values of the baseline noise of the surface electromyography were calculated, as demonstrated in Fig. 4k. The gel damper electrodes exhibited extraordinary immunity to surrounding environmental noise caused by low-frequency mechanical noise. The EMG signals recorded during the vibration have the same waveforms as those obtained in the static state, represented by a relatively constant low baseline noise of 0.07 mV. In contrast, incorporating vibration considerably deteriorated the fidelity of the EMG signals from the commercial 3 M electrodes. The baseline noise increased from 0.07 to 0.52 mV, where the SNR decreased drastically from 25.96 to 9.26 dB. The damper's behaviour offered an effective solution to the issue of motion artifacts, enabling stable electrical signal acquisition even in the presence of low-frequency mechanical noise. The physical filter of a gel damper helped in isolating the target physiological signals of interest and minimizing the influence of unwanted frequencies, resulting in cleaner and more focused signal acquisition.

2.4 Damper integrated vibration sensor system

Spider-inspired gel damping materials helped maintain the stability and reliability of the sensors. In addition, gel damping provided a degree of isolation from the surrounding environment, minimizing the influence of external factors on signal acquisition. It impeded the transmission of external motion artifacts and low-frequency mechanical noise, thereby enhancing the purity and reliability of the obtained signals. To apply a prepared gel damper to the acquisition of clear mechanical biophysiological signals, we further integrated the gel damper with a crack-based vibration sensor. The integrated damping sensor adheres tightly to the mechanical vibration testing platform using its adhesive properties (Fig. 5a). A vibration platform was used to test the response of the integrated sensor to mechanical vibrations at different frequencies to explore the frequency selectivity of the damping material and the anti-interference capability of the sensor. Vibration amplitudes were transmitted through the gel damper and PDMS reference with 10 seconds of excitation (5 and 100 Hz). As illustrated in Fig. 5b and c, when PDMS was used as a damping material, it can be employed to transmit frequency vibration signals from beam to crack sensor. Irrespective of the frequency range of the vibrational stimuli, the crack sensor demonstrated the capacity to detect signals (5 Hz and 100 Hz).

Hence, the PDMS damper-integrated sensor is significantly influenced by low-frequency vibrations and is usually overwhelmed by excessive mechanical noise in practical applications.
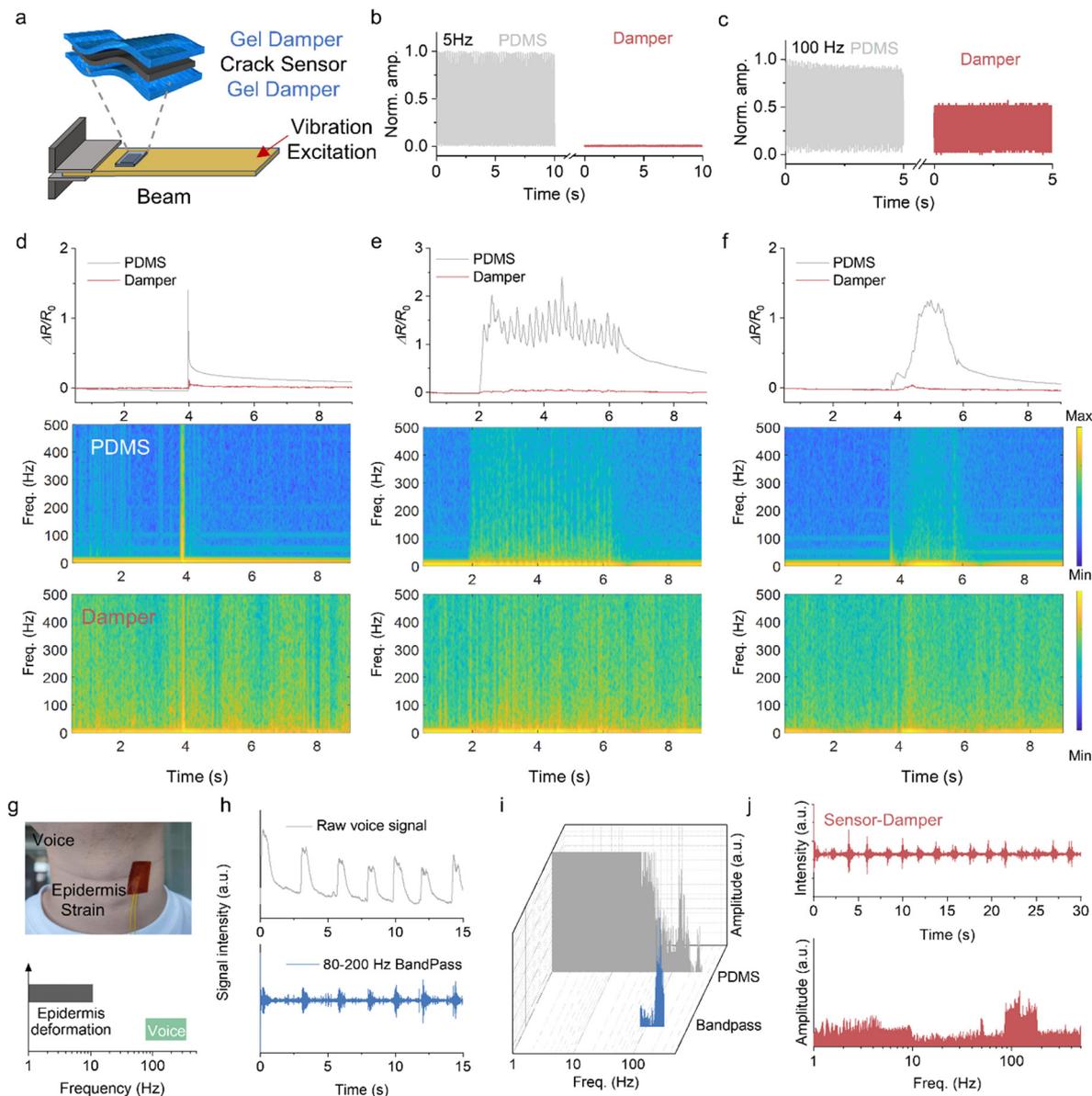
Fig. 5 Gel damper-integrated vibration sensor system. (a) Illustration images of the crack sensor integrated with two gel dampers in the vibration response. Normalized time-dependent vibration waveforms of PDMS and the gel damper samples with applied (b) 5 and (c) 100 Hz frequencies. Electrical response signal of the crack-based sensor when integrated with the gel damper (PDMS as a reference) examined under various potential noise conditions on the skin: (d) poking, (e) rubbing, and (f) pressing. (g) Demonstration of speech recording based on voice vibration using gel damper-integrated crack sensor (PDMS as reference). (h) Acquisition of acoustic signals by reference with bandpass at 80–200 Hz. (i) Fast Fourier transform (FFT) of the corresponding voice signal. (j) Acquisition of acoustic signals by a crack sensor integrated with the gel damper and the corresponding FFT signal.

By contrast, when the gel damper was applied to the integrated sensor that experiences low-frequency mechanical vibrations (5 Hz), it can effectively absorb and dissipate the mechanical energy associated with those vibrations (Fig. S35, ESI†). The damping process converts the mechanical energy into bond energy between the polymer chains, thereby reducing the amplitude and intensity of the vibrations. However, when the applied frequency was increased, it could transfer the vibrations and maintain the amplitude of the vibrations. As shown in Figure R4, the sensing system could not effectively reduce mechanical noise beyond 100 Hz, and high-frequency signals can be acquired

clearly. It was speculated that the damping gel appeared as rigid behaviour during vibration processes at 300 Hz and 500 Hz with a sharp increase in modulus, effectively transmitting the load. Therefore, the sensing system is primarily designed to isolate low-frequency mechanical noise and motion artifacts that are commonly encountered daily and cannot effectively filter out high-frequency noise.

In particular, the flexible sensor usually has dynamic mechanical noise resulting from skin tension or movement, which contributes over a broad frequency range because the noise can generate varying scales of friction. These skin

movements can create strain signals in the flexible sensor that are often of larger amplitude compared to the genuine target signals. By reducing mechanical contact and vibration interference between the sensors and the external environment, gel damping mitigates stress and deformation of the sensors, thus improving the overall stability performance. As demonstrated in Fig. 5d–f, the integrated sensor adhered to the skin and experienced rapid skin movements that involved causing friction and compression over a short period. Instantaneous movements caused significant damping deformation, resulting in signal fluctuations in the sensor. In the relative resistance change signal of the PDMS-integrated sensor, external mechanical stimulation induced substantial signal variations, while such variations were noticeably suppressed in the gel-damped sensor. The corresponding analysis of Morelet wavelet transforms of the gel damper-integrated sensor showed that the low-frequency noise components introduced by mechanical stimulation were dissipated, leading to a more stable and accurate sensor output.

During speech, the frequency of throat vibration, also known as fundamental frequency or pitch, is typically at least 100 Hz or higher. This frequency corresponds to the rate at which the vocal folds cause air to vibrate, producing the fundamental pitch of the voice. In addition, physical noise that arises from neck behaviours such as epidermis deformation or skin tension due to movement tends to have lower frequencies, typically below 30 Hz. (Fig. 5g) These lower-frequency motions can generate sounds or vibrations that are perceptible to some extent but are generally not related to the fundamental pitch of speech. In many reported cases of flexible sensors used for sound signal capture, strain signals generated by skin movement tend to have larger amplitudes compared to genuine audio signals generated by air vibrations from the throat. When sound is produced, such as during speech or vocalization, air vibrations from the throat create sound waves that propagate through the surrounding medium, including the skin. However, owing to the strain transfer between the sensor and the skin, the sensor also picks up the mechanical movements and vibrations generated by the skin. Consequently, the skin-generated signals can overshadow or mask desired audio signals, making it difficult to accurately capture and distinguish true sound information.

To verify this phenomenon, a series of voice data was recorded by no damper crack sensors attached to the neck of a volunteer. We measured phonation using ''by'' on the neck, acquired an electrical signal and performed a bandpass filtering analysis of crack sensors. As demonstrated in Fig. 5h, the raw voice signals vary obviously when the volunteer continuously pronounced the words ''by'. Moreover, the collected raw acoustic signals consist of both low-frequency cutaneous motion signals and high-frequency vocal vibration signals. After bandpass filtering is applied to the aforementioned raw acoustic signals, the low-frequency cutaneous motion signals can be attenuated, while the high-frequency vocal vibration signals can be retained. It is possible to extract genuine vocal vibration signals. Consequently, the filtered signals more accurately reflect the vibrational patterns of the vocal folds,

enabling the analysis of the frequency, intensity, and temporal characteristics of vocal vibrations with greater precision. Simultaneously, as illustrated in Fig. 5i, performing the Fourier transform on the raw voice signals yields their frequency spectra. The collected raw voice signals exhibited a predominant frequency concentration below 30 Hz and in the range of 80–200 Hz. This frequency distribution indicates that voice signals have significant energy and carry important information primarily in the low-frequency and high-frequency ranges. Frequencies below 30 Hz may involve low-frequency components related to vocal fold epidermis vibration and respiratory processes. The frequency ranging from 80 to 200 Hz likely encompasses the fundamental frequency and harmonic components of the speech signal, which play a crucial role in intonation and voice characteristics. Hence, through the application of bandpass filtering to the raw acoustic signals, it becomes possible to extract genuine vocal vibration signals, which in turn aids in further acoustic analysis and speech research.

Although signal acquisition through high-precision vibration sensors and signal processing with band-pass filter algorithms can provide the desired sound information, incorporating dampers or physical filters in conjunction with the sensors can significantly enhance the efficiency of signal acquisition. As illustrated in Fig. 5j, a voice signal from a male pronounced ''hello'' was obtained after attaching the integrated damper sensor to his neck. The acoustic signal waveform of the integrated sensor showed a marked difference between the phonation and relaxation periods. The signals collected by the damped integrated sensor exhibit typical characteristics of voice signals, which differ from the epidermis movements that are often of larger amplitude compared to genuine audio signals. By employing a fast Fourier transform (FFT), the spectrogram of the crack sensor with the gel damper exhibited a relatively distinct separation between the voice signals and the epidermis movement or breathing signal. The main frequency of the sound signal was primarily concentrated in the range of 80–200 Hz, and the low-frequency interference vibration signal was significantly attenuated.

3. Conclusion

In summary, a gel damper-integrated crack sensor was developed based on the vibration response of a spider slit organ. The crack sensor demonstrated excellent sensing performance with a low detection limit, ultrafast response time, and superior durability. Additionally, the gel damper's frequency-dependent behavior further improved the signal acquisition ability, enabling the acquisition of biophysiological signals with a high SNR in noisy or motion states. Integrating the gel damper with the crack-based sensor resulted in superior anti-interference capability and target frequency selectivity. This integrated sensor effectively extracted genuine vocal vibration signals, demonstrating its potential to enhance acoustic analysis and speech research. Overall, the integration of damping materials with sensors offers a promising approach to improving signal quality in various applications.

4. Experimental section

4.1 Materials

Ti_3AlC_2 was purchased from XFNANO. Lithium fluoride (LiF) was purchased from Shanghai Aladdin, Chain. Acrylamide monomers and Acrylic acid (AAc, 98%) were purchased from Tansoole, and gelatin powder (Gel, bloom ~100) was purchased from Shanghai Macklin Biochemical Co., Ltd. Thermoplastic polyurethane and other materials were obtained from local suppliers.

4.2 Manufacture of Mxene@TPU crack sensor

Electrospinning TPU film was subjected to oxygen plasma treatment to enhance its hydrophilicity. Then, the MXene flakes were applied to the TPU fibrous film through a vacuum filtration process. The MXene@TPU film was washed and dried. Cracks were fabricated on the MXene@TPU film surface after bending the whole film with a 1 cm curvature rod.

4.3 Preparation of the gel damper

To synthesize the gel damper, a gelatin solution was mixed by combining 20 mL of various components. These included 6 wt% gelatin, 5 wt% acrylic acid, 15 wt% acrylamide monomers, a crosslinking agent and photoinitiator. The montmorillonite was gradually added to the precursor solution and stirred continuously. Thorough mixing was ensured to distribute the montmorillonite particles evenly throughout the solution. Following vacuum degassing of the gel precursor, the polymerization process occurred.

4.4 Quasi-static electromechanical response measurements

The crack sensor was clamped by applying a universal material test machine (AG-X plus, SHIMADZU) and stretched by exact strain and force. The measurement equipment of a digital SourceMeter (Keithley 2450, Tektronix) was used to record the output signal generated by the crack sensor.

4.5 Vibration measurement and control system

The system was established to evaluate the vibration sensor that can accurately measure tiny high-frequency vibrations induced by dynamic loading. A data acquisition system was then configured to receive and record signals from the vibration sensor (3404FRS-DY, UTEKL and Keithley 2450, Tektronix). A control system was designed to simulate dynamic stimulation achieved through an excitation source (Waveform Generator, RIGOL), drive circuitry (YE1311, UTEKL), and vibration exciter (JZ-1, UTEKL) that can generate the desired vibration signal. The vibration sensor was placed on the carbon fiber beam being tested by ensuring proper contact with the sample surface, while the data acquisition system recorded real-time vibration signals from the sensor output. Finally, the recorded data were analyzed and evaluated, allowing the assessment of the performance of the vibration sensor in detecting dynamic stimulation by comparing its vibration response to that of an accelerometer (Bruel-Kjaer DeltaTron 4520-001). This system generates a controlled vibration signal using an excitation source, drive circuitry, and a mechanical device that can produce the desired dynamic vibrations.

4.6 Damping characteristics of the material

Dynamic mechanical testing was implemented by applying a dynamic mechanical analyzer (DMA Q800a, TA Instrument) in compression mode for the specific strain, and the frequency was swept from 1 Hz to 100 Hz at 25 °C. For the drop-ball experiments, the damper gel, D3O and PDMS were placed at a controlled ambient temperature of 25 °C. The experimental process involves steel balls that impact a damping material through a free fall motion. An accelerometer (Bruel-Kjaer DeltaTron 4520-001) was attached to a stainless-steel substrate to collect impact signals.

4.7 Electrophysiological signals recordings

Electrode-skin interface impedance was investigated using an Electrochemical Workstation (Zahner). Commercial 3 M monitoring electrodes (2223H, 3 M) were used in this study. The Ag/AgCl gel was separated from the electrode and replaced with the hydrogel damper of the same dimensions (1.5 cm × 1.5 cm × 2 mm). The damper electrodes were connected to the volunteer, and the ECG signal was obtained using a biopotential Recorder IX-BIO3 (Iwork Systems Inc.). For the ECG measurement, damper electrodes were attached to the right arm, left arm, and left leg of the chest. The measurement was implemented under specific noises such as walking, stretching and 6–7 Hz tapping. The EMG measurement setup was the same as the ECG measurement setup. Electrophysiological signals were acquired at 2000 Hz sampling speed by LabScribe (Iwork Systems Inc.). Signal-noise-rate was calculated with the following equation:

$$\text{SNR(dB)} = 20 \times \log_{10} \frac{\sqrt{\sum_{k=1}^{N} V_{\text{signal}(k)}^2}}{\sqrt{\sum_{k=1}^{N} V_{\text{noise}(k)}^2}},$$

where N denotes the testing frequency, and V_{signal} and V_{noise} denote the voltage of the muscle response and background or mechanical vibration noise, respectively.

Volunteers participated in this proof-of-concept demonstration with a full understanding of the process and any risks involved. Volunteers signed consent to participate in sensor test experiments.

Conflicts of interest

The authors declare no competing financial interest.

Acknowledgements

References

1 F. Ershad, S. Patel and C. Yu, *npj Flexible Electron.*, 2023, **7**, 32.

2 H. Yuk, B. Lu and X. Zhao, *Chem. Soc. Rev.*, 2019, **48**, 1642–1667.

3 Y. Hong, B. Wang, Z. Long, Z. Zhang, Q. Pan, S. Liu, X. Luo and Z. Yang, *Adv. Funct. Mater.*, 2021, **31**, 2104737.

4 Y. Song, H. Chen, X. Chen, H. Wu, H. Guo, X. Cheng, B. Meng and H. Zhang, *Nano Energy*, 2018, **53**, 189–197.

5 Y. Ma, Y. Yue, H. Zhang, F. Cheng, W. Zhao, J. Rao, S. Luo, J. Wang, X. Jiang, Z. Liu, N. Liu and Y. Gao, *ACS Nano*, 2018, **12**, 3209–3216.

6 D. Sun, Y. Feng, S. Sun, J. Yu, S. Jia, C. Dang, X. Hao, J. Yang, W. Ren, R. Sun, C. Shao and F. Peng, *Adv. Funct. Mater.*, 2022, **32**, 2201335.

7 B. Yiming, Y. Han, Z. Han, X. Zhang, Y. Li, W. Lian, M. Zhang, J. Yin, T. Sun, Z. Wu, T. Li, J. Fu, Z. Jia and S. Qu, *Adv. Mater.*, 2021, **33**, 2006111.

8 J. Zou, X. Jing, Z. Chen, S. J. Wang, X. S. Hu, P. Y. Feng and Y. J. Liu, *Adv. Funct. Mater.*, 2023, **33**, 2213895.

9 C. Zhang, H. Zheng, J. Sun, Y. Zhou, W. Xu, Y. Dai, J. Mo and Z. Wang, *Adv. Mater.*, 2022, **34**, 2105996.

10 K. Zhao, J. Yang, M. Zhong, Q. Gao, Y. Wang, X. Wang, W. Shen, C. Hu, K. Wang, G. Shen, M. Li, J. Wang, W. Hu and Z. Wei, *Adv. Funct. Mater.*, 2021, **31**, 2006601.

11 B. Park, J. H. Shin, J. Ok, S. Park, W. Jung, C. Jeong, S. Choy, Y. J. Jo and T. I. Kim, *Science.*, 2022, **376**, 624–629.

12 K. H. Lee, X. Ni, J. Y. Lee, H. Arafa, D. J. Pe, S. Xu, R. Avila, M. Irie, J. H. Lee, R. L. Easterlin, D. H. Kim, H. U. Chung, O. O. Olabisi, S. Getaneh, E. Chung, M. Hill, J. Bell, H. Jang, C. Liu, J. Bin Park, J. Kim, S. B. Kim, S. Mehta, M. Pharr, A. Tzavelis, J. T. Reeder, I. Huang, Y. Deng, Z. Xie, C. R. Davies, Y. Huang and J. A. Rogers, *Nat. Biomed. Eng.*, 2020, **4**, 148–158.

13 Y. Politi, L. Bertinetti, P. Fratzl and F. G. Barth, *Philos. Trans. R. Soc., A*, 2021, **379**, 20200332.

14 T. Kim, I. Hong, Y. Roh, D. Kim, S. Kim, S. Im, C. Kim, K. Jang, S. Kim, M. Kim, J. Park, D. Gong, K. Ahn, J. Lee, G. Lee, H. S. Lee, J. Kang, J. M. Hong, S. Lee, S. Seo, B. K. Koo, J. S. Koh, S. Han and D. Kang, *npj Flexible Electron.*, 2023, **7**, 12.

15 D. Kang, P. V. Pikhitsa, Y. W. Choi, C. Lee, S. S. Shin, L. Piao, B. Park, K. Y. Suh, T. I. Kim and M. Choi, *Nature*, 2014, **516**, 222–226.

16 X. Liu, D. Liu, J. H. Lee, Q. Zheng, X. Du, X. Zhang, H. Xu, Z. Wang, Y. Wu, X. Shen, J. Cui, Y. W. Mai and J. K. Kim, *ACS Appl. Mater. Interfaces*, 2019, **11**, 2282–2294.

17 Y. Zhao, W. Gao, K. Dai, S. Wang, Z. Yuan, J. Li, W. Zhai, G. Zheng, C. Pan, C. Liu and C. Shen, *Adv. Mater.*, 2021, **33**, 2102332.

18 H. Zhang, H. Chen, J. H. Lee, E. Kim, K. Y. Chan, H. Venkatesan, X. Shen, J. Yang and J. K. Kim, *ACS Nano*, 2023, **17**, 5921–5934.

19 J. Huang, A. Chen, S. Han, Q. Wu, J. Zhu, J. Zhang, Y. Chen, J. Liu and L. Guan, *Adv. Sci.*, 2023, 2301116.

20 C. S. Boland, U. Khan, G. Ryan, S. Barwich, R. Charifou, A. Harvey, C. Backes, Z. Li, M. S. Ferreira, M. E. Möbius, R. J. Young and J. N. Coleman, *Science*, 2016, **354**, 1257–1260.

21 H. Xiang, X. Li, B. Wu, S. Sun and P. Wu, *Adv. Mater.*, 2023, **35**, 2209581.

22 L. Liu, S. Niu, J. Zhang, Z. Mu, J. Li, B. Li, X. Meng, C. Zhang, Y. Wang, T. Hou, Z. Han, S. Yang and L. Ren, *Adv. Mater.*, 2022, **34**, 2200823.

23 S. L. Young, M. Chyasnavichyus, M. Erko, F. G. Barth, P. Fratzl, I. Zlotnikov, Y. Politi and V. V. Tsukruk, *Acta Biomater.*, 2014, **10**, 4832–4842.

24 B. Park, J. Kim, D. Kang, C. Jeong, K. S. Kim, J. U. Kim, P. J. Yoo and T. I. Kim, *Adv. Mater.*, 2016, **28**, 8130–8137.

25 K. Tian, J. Bae, S. E. Bakarich, C. Yang, R. D. Gately, G. M. Spinks, M. in het panhuis, Z. Suo and J. J. Vlassak, *Adv. Mater.*, 2017, **29**, 1604827.

26 J. Huang, S. Peng, J. Gu, G. Chen, J. Gao, J. Zhang, L. Hou, X. Yang, X. Jiang and L. Guan, *Mater. Horiz.*, 2020, **7**, 2085–2096.

27 J. Huang, J. Gu, J. Liu, J. Guo, H. Liu, K. Hou, X. Jiang, X. Yang and L. Guan, *J. Mater. Chem. A*, 2021, **9**, 16345–16358.

28 E. Choi, H. Youn, K. Park and J. S. Jeon, *Eng. Struct.*, 2017, **132**, 372–382.

29 C. Wang, X. Chen, L. Wang, M. Makihata, H. Liu, T. Zhou and X. Zhao, *Science*, 2022, **377**, 517–523.

30 G. Yang, K. Zhu, W. Guo, D. Wu, X. Quan, X. Huang, S. Liu, Y. Li, H. Fang, Y. Qiu, Q. Zheng, M. Zhu, J. Huang, Z. Zeng, Z. Yin and H. Wu, *Adv. Funct. Mater.*, 2022, **32**, 2200457.